frontiers in Earth Science

ORIGINAL RESEARCH
published: 30 April 2021
doi: 10.3389/feart.2021.607695

Modern Sedimentation and Authigenic Mineral Formation in the Chew Bahir Basin, Southern Ethiopia: Implications for Interpretation of Late Quaternary Paleoclimate Records

Daniel Gebregiorgis[1], Daniel M. Deocampo[1], Verena Foerster[2], Fred J. Longstaffe[3], Jeremy S. Delaney[4], Frank Schaebitz[2], Annett Junginger[5], Monika Markowska[6], Stephan Opitz[7], Martin H. Trauth[8], Henry F. Lamb[9,10] and Asfawossen Asrat[11]*

[1] Department of Geosciences, Georgia State University, Atlanta, GA, United States, [2] Institute of Geography Education, University of Cologne, Cologne, Germany, [3] Department of Earth Sciences, The University of Western Ontario, London, ON, Canada, [4] Department of Earth and Planetary Sciences, Rutgers University, Piscataway, NJ, United States, [5] Department of Geosciences, University of Tübingen, Tübingen, Germany, [6] Department of Climate Geochemistry, Max Planck Institute for Chemistry, Mainz, Germany, [7] Institute of Geography, University of Cologne, Cologne, Germany, [8] Institute of Geosciences, University of Potsdam, Potsdam, Germany, [9] Department of Geography and Earth Sciences, Aberystwyth University, Aberystwyth, United Kingdom, [10] Botany Department, School of Natural Sciences, Trinity College, Dublin, Ireland, [11] School of Earth Sciences, Addis Ababa University, Addis Ababa, Ethiopia

OPEN ACCESS

Edited by:
Gary E. Stinchcomb,
Murray State University, United States

Reviewed by:
Steven L. Forman,
Baylor University, United States
Dhananjay Anant Sant,
Maharaja Sayajirao University of Baroda, India

***Correspondence:**
Daniel Gebregiorgis
dgebregiorgis@gsu.edu

Specialty section:
This article was submitted to Quaternary Science, Geomorphology and Paleoenvironment, a section of the journal Frontiers in Earth Science

Received: 17 September 2020
Accepted: 24 March 2021
Published: 30 April 2021

Citation:
Gebregiorgis D, Deocampo DM, Foerster V, Longstaffe FJ, Delaney JS, Schaebitz F, Junginger A, Markowska M, Opitz S, Trauth MH, Lamb HF and Asrat A (2021) Modern Sedimentation and Authigenic Mineral Formation in the Chew Bahir Basin, Southern Ethiopia: Implications for Interpretation of Late Quaternary Paleoclimate Records. Front. Earth Sci. 9:607695. doi: 10.3389/feart.2021.607695

We present new mineralogical and geochemical data from modern sediments in the Chew Bahir basin and catchment, Ethiopia. Our goal is to better understand the role of modern sedimentary processes in chemical proxy formation in the Chew Bahir paleolake, a newly investigated paleoclimatic archive, to provide environmental context for human evolution and dispersal. Modern sediment outside the currently dry playa lake floor have higher SiO_2 and Al_2O_3 (50–70 wt.%) content compared to mudflat samples. On average, mudflat sediment samples are enriched in elements such as Mg, Ca, Ce, Nd, and Na, indicating possible enrichment during chemical weathering (e.g., clay formation). Thermodynamic modeling of evaporating water in upstream Lake Chamo is shown to produce an authigenic mineral assemblage of calcite, analcime, and Mg-enriched authigenic illitic clay minerals, consistent with the prevalence of environments of enhanced evaporative concentration in the Chew Bahir basin. A comparison with samples from the sediment cores of Chew Bahir based on whole-rock MgO/Al_2O_3, Ba/Sr and authigenic clay mineral $\delta^{18}O$ values shows the following: modern sediments deposited in the saline mudflats of the Chew Bahir dried out lake bed resemble paleosediments deposited during dry periods, such as during times of the Last Glacial Maximum and Younger Dryas stadial. Sediments from modern detrital upstream sources are more similar to sediments deposited during wetter periods, such as the early Holocene African Humid Period.

Keywords: oxygen isotopes in authegenic clay minerals, X-ray core scanning, paleoclimate proxy formation and interpretation, whole-rock and clay mineralogy, geochemical modeling, the Chew Bahir K record

INTRODUCTION

The field of sedimentary geochemistry is at the forefront of both outcrop- and core-based paleoclimate research. Aided by the introduction of X-ray fluorescence (XRF) core scanning techniques, down-core patterns of element intensities and ratios in both marine and lake sediments are routinely applied as proxies of past climate changes (e.g., Croudace et al., 2006, 2019; Lyons et al., 2015; Gebregiorgis et al., 2020b). Although the link between the chemistry of deposited weathering products and climate is complex, the distribution of mobile versus immobile elements in sediment likely varies in accordance with climate variables (e.g., temperature, precipitation; e.g., Harriss and Adams, 1966; Nesbitt, 1979; Chesworth et al., 1981; Middelburg et al., 1988). Element intensities (e.g., Zr, Ti, K) and ratios (e.g., K/Zr, K/Ti, K/Al, and K/Rb) are routinely used to trace a wide range of climate-related processes such as changes in rainfall amount (e.g., Foerster et al., 2012; Hendy et al., 2015) and intensity of weathering processes (e.g., Burnett et al., 2011; Tian et al., 2011; Clift et al., 2014) within lake catchments.

The application of XRF-generated elemental proxies in paleoclimatology, however, is not without its pitfalls. Depositional variability, hiatuses and erosion, diagenesis, and pedogenesis commonly work together to obscure or overprint primary geochemical signals preserved in sediments. Authigenic mineral formation can also control lake sediment geochemistry, particularly in saline lakes (Deocampo and Jones, 2014). Indeed, in many African lakes, clay minerals rich in Al, or zeolites rich in Ca or K, have been shown to alter in saline and alkaline lakes to produce Mg-rich authigenic clay minerals and Na-rich analcime (e.g., Surdam and Eugster, 1976; Singer and Stoffers, 1980; Trauth et al., 2001; Deocampo, 2004, 2015). As a result, large discrepancies between lake records remain unresolved, leading to difficulties in interpreting proxy records of climate (e.g., Trauth et al., 2003). These challenges are in large part due to an incomplete understanding of proxy formation and are particularly relevant in paleolimnology, where down-core variability of selected elements in the sediment may have little direct relation with the rate and intensity of weathering of the surrounding catchment, but might rather reflect post-depositional hydrochemical conditions.

The potassium (K) record of the Chew Bahir basin provides an excellent example demonstrating the complexity of interpreting highs and lows in K content in the sediment as past water balance changes in the catchment (Foerster et al., 2012; Fischer et al., 2020). Foerster et al. (2018) considered multiple hypotheses to explain the K record, concluding that K enrichment in the sediment could not entirely indicate episodes of enhanced detrital input, but rather incipient low temperature K-fixation during illitization associated with Mg uptake and clay mineral layer charge increase (Deocampo and Tactikos, 2010; Deocampo, 2015). It is worth noting that the temporal variability of the K record is remarkably consistent with half a dozen well-dated proxy records from continental Africa (e.g., Brown et al., 2007; Junginger and Trauth, 2013; Tierney and deMenocal, 2013; Otto-Bliesner et al., 2014; Shanahan et al., 2015).

The present study takes its impetus from Foerster et al. (2018) and has three main objectives. The study's core objective is to describe the major input and alteration processes utilizing new geochemical data in modern sediments collected from the Chew Bahir basin. Second, by comparing the new geochemical data from the modern sediments with PHREEQC geochemical modeling, where the acronym PHREEQC stands for PH (pH), RE (redox), EQ (equilibrium), and C (program written in C), of local waters, the study aims to improve our understanding of relevant hydrogeochemical processes in the Chew Bahir catchment. Third, the study aims to further refine interpretations of the Chew Bahir K record using clay mineralogical and geochemical analysis of modern sediments collected from the Chew Bahir catchment. Within this framework, this study is aimed at advancing our understanding of such climate proxies, and the development of a reliable high-resolution environmental context for the newly investigated site of Chew Bahir. A preliminary attempt is made to investigate whether oxygen-isotope measurements of authigenic clay minerals covering notable warm/wet (e.g., the early-middle Holocene) and cold/dry intervals (e.g., the Last Glacial Maximum, LGM) suggest similar changes in wet and dry conditions inferred from the Chew Bahir K record.

GEOMORPHOLOGY OF THE CHEW BAHIR BASIN

The Chew Bahir basin is a hydrographic and sedimentary system located at the southern sector of the Main Ethiopian Rift, northeast of the Omo-Turkana basin of southern Ethiopia and northern Kenya (**Figures 1a–d**). It forms part of a ∼250 km wide broadly rifted zone, mainly composed of Pliocene-Holocene sediment-filled basins underlying strongly uplifted Precambrian blocks (e.g., Ebinger et al., 2000). Oligocene basalts and subordinate rhyolites, trachytes, tuffs and ignimbrites cover the Precambrian basement units near the northeastern, northern and northwestern parts of the catchment. The Teltele plateau, which consists of Miocene basalts and rhyolite, trachyte and felsic tuff, is located in the eastern part of the Chew Bahir catchment (**Figure 1d**; see also Davidson, 1983). The northern part of the Teltele plateau extends to the Konso upland, which is drained by the Segen River, one of the major rivers draining to the Weyto River, and then to the Chew Bahir basin (Fischer et al., 2020).

The Chew Bahir basin is a deep tectonic basin, where a nearly flat, ∼30 km wide and ∼100 km long playa surface is bounded by a ∼500 m high tectonic escarpments to its west and east. Formation of shallow but wide alluvial fans, the biggest of which is a 20 km by 10 km fan located just west of the Chew Bahir coring sites, has been the major geomorphological features at the borders between the basin and the adjacent highland graben shoulders. The Weyto River flows in a north-south direction, forming a wide and shallow deltaic system before it disappears into the playa wetland (**Figure 1c**). The northern part of the flat basin is covered by relatively dense grassland vegetation mostly inhibiting aeolian geomorphological processes. Only on the vegetation-free, strongly desiccated southernmost (∼20 km long) part of the basin can local aeolian deflation, remobilization and sedimentation of

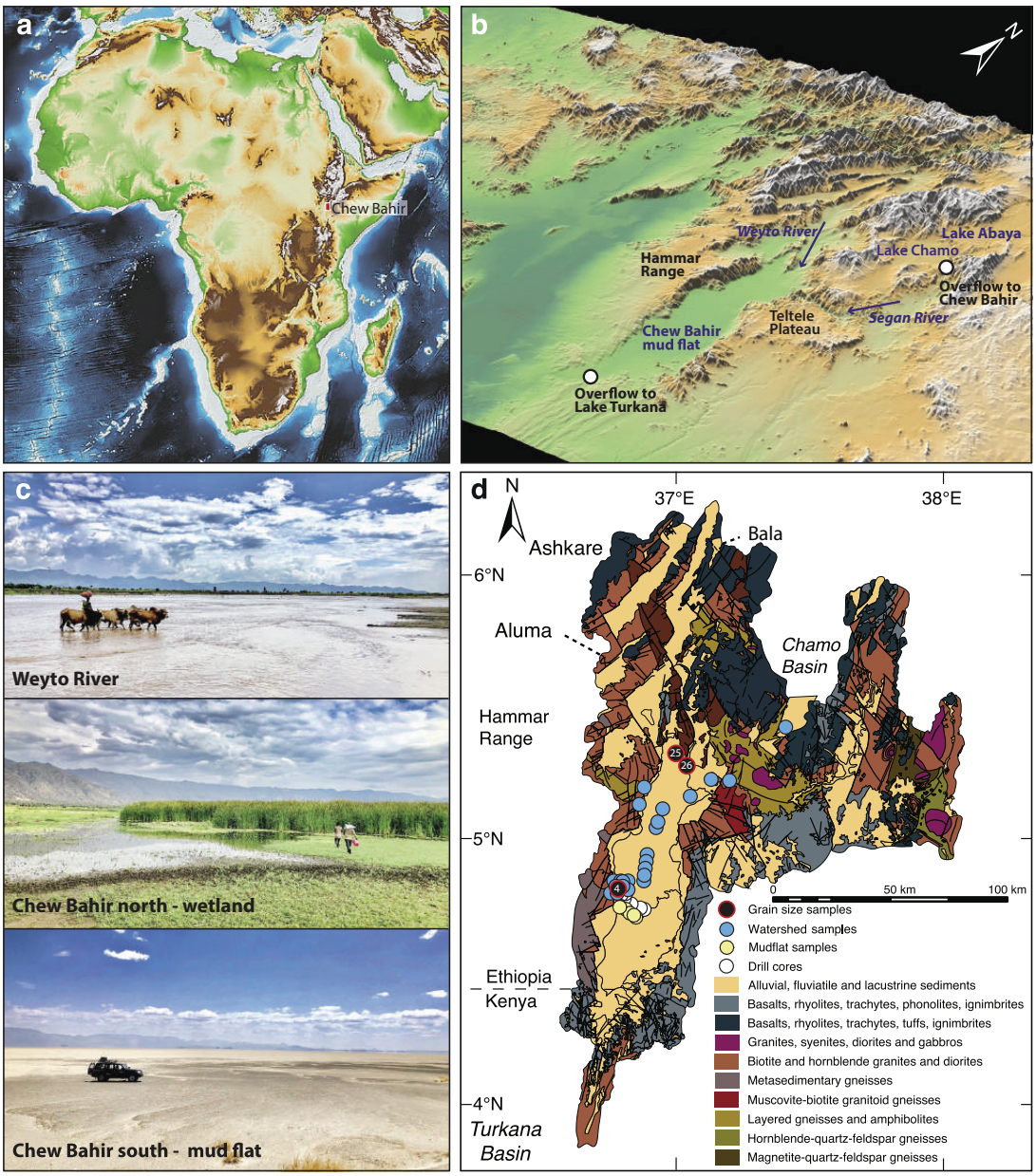

FIGURE 1 | Elevation map of **(a)** eastern Africa with **(b)** 3D, **(c)** field, and **(d)** geologic representation of the Chew Bahir basin. Filled blue and yellow-green circles in **(d)** show sampling locations for modern watershed (WS) and mudflat (MF) samples, respectively. Filled black circles in **(d)** show locations of samples collected from the Chew Bahir catchment for grain size analysis.

fine sediments by "dust-devils" or dust storms be observed. In the extreme southern part of the Chew Bahir basin, small aeolian geomorphological features like "kupsten" dunes appear close to the recent "coastline."

The Chew Bahir tectonic basin, which has an elevation of ∼500 masl, lies on the southeastern side of the western Ethiopian highlands, which are greater than ∼2,500 masl (**Figures 1a,b**). The deep basin is thus located on the lee of potential dust sources, especially the Sahara. Likewise, the ∼1,800 m high Teltele plateau, which gently descends to the east, blocks potential dust plumes from reaching the southeastern Ethiopian lowlands. The paleo-lake 'periodically fills with water (up to 2 m in depth) supplied primarily via the Weyto River. Modern dust input in the form of local short events of "dust-devils" occurs during remobilization and deposition of dust from the loose playa sediments on the strongly desiccated surface in the extreme southern part of the basin.

In sum, the Hammar Range to the west and the highlands to the north and northeast, consisting of Late Proterozoic granite and gneiss, are therefore the primary sediment sources to the Chew Bahir basin (Foerster et al., 2012). All surface samples were therefore collected between sub-watersheds from riverbeds or the

desiccated lake floor to help improve our understanding of proxy formation in this region (see sampling locations in **Figure 1d** and methods). However, it should be noted that our study cannot be considered an exhaustive survey of all geomorphological processes active in the larger Chew Bahir catchment.

HYDROGEOLOGICAL AND CLIMATIC FEATURES OF THE CHEW BAHIR CATCHMENT

Today the Chew Bahir basin and catchment area has two rainy seasons, during boreal spring and autumn, owing to the North–South migration of the tropical African rain belt (**Figures 2a–c**). The tropical African rain belt is commonly referred to as the intertropical convergence zone (ITCZ) but the twice-yearly passing of the tropical African rain belt may not necessarily be synchronized with the annual cycle of insolation (e.g., Nicholson, 2018). Catchment wide mean annual rainfall is in the order of 900–1,000 mm, and the boreal spring rainy season (i.e., March–May) accounts for >50% of the annual total (Fischer et al., 2020).

Water balance model estimates for paleo-lake Chew Bahir, based on the Surface Energy Balance Algorithm for Land, estimate an actual evaporation rate for the catchment of 847 mm/a (Fischer et al., 2020). Although mesoscale convective processes and topography also play an important role in the development of rain-bearing systems in eastern Africa (e.g., Hession and Moore, 2011), aridity in the catchment area is linked to large-scale divergence in the lower troposphere (Nicholson, 2016). The prevailing aridity in northern Kenya and southern Ethiopia is also associated with the Turkana Jet, which flows at low levels with highest wind speeds at the 850 mb pressure level; maximum aridity over the region occurs when the Turkana Jet is at minimum speed (Nicholson, 2016). There is also a negative correlation between the strength of the Turkana Jet and low level divergence, and rainfall over that region (e.g., Sun et al., 1999). On a broader scale, rainfall patterns in eastern Africa are also sensitive to sea surface temperature variability in both the Indian and Pacific Oceans (e.g., Gebregiorgis et al., 2019).

During the last African Humid Period (AHP), 20–30% more precipitation led to lake level rises of Lake Abaya-Chamo (Fischer et al., 2020). At that time, overflow spilled into the Chew Bahir basin forming paleo-lake Chew Bahir, which in turn overspilled into Lake Turkana after reaching the overflow sill at 543 masl (Fischer et al., 2020).

MATERIALS AND METHODS

Sampling

Thirty-four surface samples from the main catchment areas of paleo-lake Chew Bahir were collected in October 2018 for mineralogical, and major, minor and trace element analyses (**Table 1**). Twenty-eight of these surface samples were collected between watersheds from riverbeds (henceforth referred to as watershed samples or WS samples). Six samples were collected from the desiccated lake floor (henceforth referred to as mudflat samples or MF samples). Twelve samples from the Chew Bahir pilot drill core CB-01 were analyzed from selected wetter and drier intervals of the late Pleistocene and Holocene based on the Chew Bahir K record (**Figure 3**; Foerster et al., 2012, 2018). Samples collected from wetter intervals (henceforth referred to as WI) include 6 samples from the AHP interval, ∼15–5 ka (Demenocal et al., 2000; Shanahan et al., 2015). Samples collected from drier intervals (henceforth referred as DI) include 2 samples each from the LGM (∼21 ka BP; Clark et al., 2009), Younger

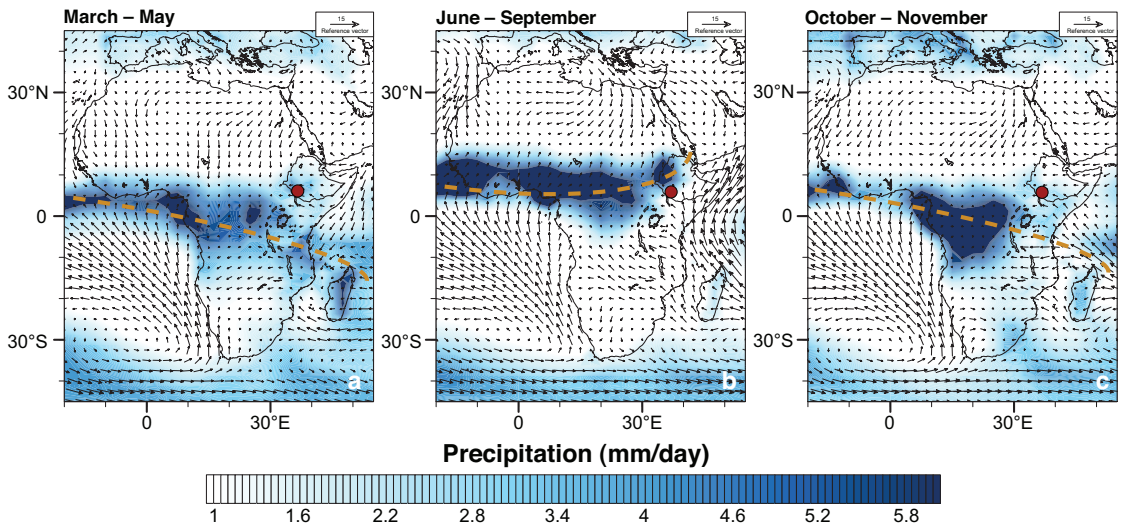

FIGURE 2 | Seasonal precipitation (mm/day) patterns in eastern Africa during **(a)** March–May, **(b)** June–September, and **(c)** October–November; mean precipitation for the period 1979–2015 at 1,000 hPa geopotential height (gph) fields. Global Precipitation Climatology Centre (GPCC) monthly precipitation data is acquired from the National Oceanic and Atmospheric Administration (NOAA) and can be accessed at https://www.esrl.noaa.gov/psd/. Thick, dashed, brown lines indicate the approximate location of the tropical African rain belt. Red circle indicates the location of the drill site.

TABLE 1 | Major/minor (wt. %) and trace (including rare earth) (ppm) element compositions of modern and down-core Chew Bahir samples.

Legend	WS1	WS2	WS3	WS4	WS5	WS6	WS7	WS8	WS9	WS10	WS11	WS12	WS13	WS14	WS15	WS16
SiO_2†	68.7	64.4	62.2	59.4	60.9	56.5	61.3	60.3	58.3	55.1	54.8	68.2	61.1	56.4	56.5	60.3
Al_2O_3†	14.0	15.3	15.3	14.3	15.6	14.8	14.7	16.4	16.9	16.7	15.9	13.1	16.4	16.5	16.2	15.9
CaO†	3.9	4.4	4.8	5.9	4.6	5.0	4.7	4.6	4.7	6.4	5.2	2.7	5.1	4.7	4.3	4.1
Fe_2O_3†	4.7	5.4	6.4	7.5	7.3	11.3	9.4	7.1	6.9	6.9	7.2	5.1	6.6	7.5	6.5	7.5
K_2O†	1.8	2.1	1.9	1.9	2.3	1.9	1.9	2.2	2.3	2.2	2.1	2.7	2.0	2.3	2.2	2.0
MgO†	1.5	1.7	2.2	2.5	2.2	2.8	2.2	2.4	2.5	3.3	3.0	1.4	2.3	3.4	2.1	2.0
Na_2O†	3.4	3.4	3.4	3.0	3.5	3.2	3.3	3.6	3.7	3.7	3.6	3.3	4.0	3.2	3.9	4.1
TiO_2†	0.5	0.7	1.0	1.0	1.0	1.7	1.3	0.9	1.0	1.0	1.0	0.6	0.9	1.1	1.0	1.2
Ba	837	833	686	741	857	673	689	876	880	789	761	804	775	840	719	565
Ce	36	52	54	57	62	81	68	62	84	79	77	61	60	77	61	63
Co	9	11	15	15	15	22	17	16	17	20	20	9	15	24	17	19
Cr	40	50	50	80	60	90	80	60	70	80	80	40	60	90	60	70
Dy	3.5	5.5	5.3	5.8	5.3	7.0	5.7	5.5	6.5	6.7	6.6	7.0	5.4	6.4	5.1	6.3
Er	2.2	3.0	3.1	3.3	2.9	4.0	3.3	3.1	3.5	3.9	3.6	3.4	3.1	3.6	2.8	3.4
Eu	1.2	1.7	1.8	1.6	1.8	1.9	1.7	1.8	2.0	2.2	2.2	2.2	1.8	2.1	1.8	1.7
Ga	14.0	16.0	18.0	17.0	18.0	21.0	19.0	19.0	21.0	21.0	21.0	19.0	19.0	21.0	20.0	20.0
Gd	3.4	5.0	5.5	5.6	5.7	7.5	6.0	5.7	7.3	7.1	6.9	7.1	5.4	7.1	5.4	6.0
Hf	3.1	4.2	4.8	4.5	4.8	7.9	7.2	7.0	10.6	8.2	6.6	4.8	6.6	6.6	5.1	6.3
Ho	0.7	1.0	1.1	1.1	1.0	1.3	1.1	1.1	1.2	1.2	1.3	1.3	1.1	1.2	0.9	1.2
La	17.9	26.6	26.3	27.3	29.7	37.0	31.7	29.7	39.6	37.5	36.3	29.3	28.5	37.0	30.0	29.3
Lu	0.4	0.5	0.5	0.5	0.4	0.6	0.5	0.4	0.5	0.5	0.6	0.5	0.5	0.5	0.4	0.5
Nb	3.0	6.0	6.0	6.0	6.0	11.0	8.0	8.0	11.0	9.0	8.0	4.0	6.0	9.0	14.0	16.0
Nd	18	26	29	28	32	40	34	31	41	41	40	35	31	39	30	32
Rb	28	37	34	36	44	37	32	47	48	52	46	51	34	52	46	33
Sc	12	15	14	19	14	20	16	15	16	18	17	10	14	20	13	14
Sm	3.9	5.9	6.4	6.5	7.1	8.4	7.4	6.8	9.1	8.6	8.7	8.5	6.4	8.6	6.4	7.4
Sr	482	456	491	504	473	429	436	457	526	584	542	315	522	452	538	433
Tb	0.6	0.9	0.9	1.0	0.9	1.2	1.0	0.9	1.1	1.1	1.1	1.2	0.9	1.1	0.9	1.0
Th	2.6	3.8	3.2	4.3	4.2	5.9	5.2	4.1	5.1	3.5	3.6	4.7	3.6	5.4	3.3	3.2
Tm	0.3	0.5	0.4	0.5	0.4	0.6	0.5	0.4	0.5	0.5	0.5	0.5	0.4	0.5	0.4	0.5
U	0.4	0.7	0.5	0.7	0.5	0.7	0.6	0.6	0.8	0.7	0.7	0.5	0.5	0.7	0.6	0.8
V	82	88	101	148	119	213	175	107	107	112	119	61	107	134	95	122
Yb	2.1	3.0	2.8	3.4	2.6	3.8	3.2	2.7	3.2	3.4	3.5	3.0	2.8	3.3	2.5	3.2
Zr	126	182	186	168	197	306	282	270	410	316	264	215	259	270	200	251
CIA	60	61	60	57	60	60	60	61	61	57	59	60	60	62	61	61
Eu/Eu*	1.01	0.91	0.89	0.76	0.81	0.72	0.74	0.88	0.73	0.82	0.83	0.82	0.91	0.80	0.92	0.77

(Continued)

TABLE 1 | Continued

Legend	WS17	WS18	WS19	WS20	WS21	WS22	WS23	WS24	WS25	WS26	WS27	WS28	MF1	MF2	MF3
SiO_2†	67.0	55.5	55.4	56.2	56.5	61.8	65.2	59.4	60.1	54.4	58.3	44.9	42.4	28.9	31.4
Al_2O_3†	14.0	16.1	15.6	15.0	16.6	15.7	12.0	14.1	15.1	14.7	15.1	14.2	12.1	8.6	9.4
CaO†	3.4	7.2	4.6	6.2	4.8	4.5	4.1	5.3	7.3	9.9	7.2	8.3	8.0	14.7	15.6
Fe_2O_3†	6.2	9.5	7.6	7.5	7.7	7.1	5.4	8.8	8.1	9.0	10.1	17.2	9.3	6.4	6.9
K_2O†	2.1	1.5	2.3	2.6	2.5	2.1	2.2	2.0	1.4	0.4	0.5	1.0	2.2	1.5	1.6
MgO†	1.3	3.1	2.5	2.6	2.9	1.7	1.3	2.9	1.8	6.8	3.7	3.7	5.1	3.1	3.4
Na_2O†	3.7	3.9	3.3	3.4	4.0	4.2	2.7	3.1	3.3	2.9	2.6	2.8	4.9	11.6	6.7
TiO_2†	0.9	1.3	1.0	0.9	1.1	1.0	0.8	1.6	0.6	0.7	0.7	3.0	1.1	1.1	1.1
Ba	738	470	696	754	766	711	542	776	855	170	209	523	371	485	524
Ce	57	44	68	65	66	49	68	50	61	31	17	77	83	95	105
Co	11	22	21	19	20	13	12	23	20	24	50	36	25	16	18
Cr	50	120	80	80	90	50	50	230		770	24	100	60	50	50
Dy	4.2	5.0	6.5	5.7	6.0	4.5	5.5	4.8	5.7	5.1	4.0	6.9	7.8	8.5	8.9
Er	2.3	2.8	3.5	3.1	3.3	2.5	3.1	2.7	3.4	3.0	2.3	3.4	4.1	4.4	4.8
Eu	1.5	1.5	1.8	1.8	2.1	2.0	1.6	1.7	1.6	1.7	1.1	2.7	2.3	2.6	2.9
Ga	17.0	19.0	20.0	20.0	22.0	19.0	17.0	18.0	16.0	18.0	14.0	23.0	19.0	13.0	14.0
Gd	4.4	4.9	6.6	5.7	6.1	4.7	6.1	4.8	6.4	5.2	3.5	7.7	8.2	8.9	9.8
Hf	5.7	4.4	5.0	4.7	6.3	5.1	6.4	9.5	2.3	1.6	0.9	5.6	5.4	3.6	4.0
Ho	0.8	1.0	1.3	1.1	1.2	0.9	1.0	0.9	1.1	1.0	0.8	1.3	1.5	1.6	1.7
La	28.3	20.2	32.4	32.2	30.6	23.6	32.4	22.9	30.1	12.4	7.2	38.5	48.7	55.1	59.3
Lu	0.3	0.4	0.5	0.4	0.5	0.4	0.4	0.5	0.5	0.4	0.3	0.5	0.6	0.6	0.7
Nb	9.0	10.0	12.0	12.0	12.0	8.0	17.0	15.0	5.0	4.0	1.0	37.0	31.0	26.0	26.0
Nd	28	23	36	32	33	25	34	26	31	21	13	40	45	52	55
Rb	34	22	48	58	55	35	43	43	17	2	6	16	42	27	31
Sc	9	24	17	17	18	13	10	18	23	41	39	28	17	15	18
Sm	5.4	5.3	8.1	7.2	7.6	5.5	7.1	5.6	7.0	5.5	3.4	8.7	9.7	11.1	11.8
Sr	501	510	418	479	524	561	319	537	723	714	209	462	498	860	917
Tb	0.7	0.8	1.1	0.9	1.0	0.7	1.0	0.8	1.0	0.8	0.6	1.2	1.3	1.4	1.5
Th	4.0	2.4	3.5	3.5	3.4	2.6	4.6	4.5	0.2	0.2	0.1	3.8	5.7	5.7	6.4
Tm	0.3	0.4	0.5	0.4	0.5	0.4	0.4	0.4	0.5	0.5	0.3	0.5	0.6	0.7	0.7
U	0.5	0.5	0.7	0.7	0.7	0.4	1.2	1.8	0.2	0.1	0.1	1.2	0.8	5.0	1.8
V	96	191	111	113	128	114	79	177	90	212	1	344	134	126	119
Yb	2.0	2.7	3.4	2.7	3.0	2.4	2.8	2.9	3.4	2.8	2.2	3.1	3.6	4.1	4.1
Zr	229	171	196	175	239	199	238	357	81	50	17	228	211	147	156
CIA	60	56	60	55	60	59	57	58	56	53	60	54	44	24	28
Eu/Eu*	0.90	0.85	0.71	0.81	0.89	1.15	0.70	0.96	0.71	0.93	0.93	0.97	0.76	0.77	0.78

(Continued)

TABLE 1 | Continued

Legend	MF4	MF5	MF6	DI1	DI2	DY3	DI4	DI5	DI6	WI1	WI2	WI3	WI4	WI5	WI6
SiO_2†	37.2	39.7	45.4	35.6	40.9	40.9	41.9	44.8	42.5	44.3	43.8	49.5	41.6	45.5	36.7
Al_2O_3†	12.3	12.8	15.1	9.7	10.1	10.7	11.3	11.2	10.5	11.1	11.5	11.0	10.7	10.4	8.2
CaO†	10.5	8.6	6.1	13.4	5.4	9.5	5.8	2.6	6.2	5.2	5.2	2.0	7.8	3.3	11.6
Fe_2O_3†	8.8	9.0	9.7	7.0	8.6	8.7	9.1	10.0	8.5	8.7	9.5	8.8	8.6	8.1	6.5
K_2O†	1.7	1.8	1.8	2.3	2.9	2.4	2.4	2.8	2.3	1.9	1.6	1.3	1.3	1.6	1.1
MgO†	3.5	3.6	3.5	5.1	7.1	5.5	6.5	6.1	4.9	5.1	3.4	2.5	2.8	3.2	2.9
Na_2O†	6.0	6.5	2.7	4.6	5.0	4.3	5.5	6.0	5.8	4.9	5.0	6.3	5.4	8.4	7.8
TiO_2†	1.4	1.3	1.4	0.9	1.0	1.0	1.1	0.9	1.0	0.9	1.0	0.9	0.9	0.9	0.7
Ba	459	469	502	514	281	381	345	204	288	279	330	236	345	308	304
Ce	104	92	91	75	44	68	66	62	69	59	81	71	103	55	69
Co	24	25	26	18	24	21	23	28	23	23	23	24	20	17	14
Cr	60	70	90	60	50	50	70	90	50	60	70	70	70	50	60
Dy	9.9	8.1	7.8	6.2	3.7	5.4	4.8	4.3	5.3	4.9	6.2	5.7	7.4	4.4	5.0
Er	5.0	4.3	4.0	3.2	2.0	3.0	2.5	2.3	2.9	2.7	3.3	3.2	3.9	2.3	2.6
Eu	3.1	2.5	2.4	1.7	1.0	1.5	1.4	1.1	1.5	1.4	1.6	1.6	1.9	1.2	1.4
Ga	19.0	19	22	14	15	15	16	18	16	16	17	18	16	12	12
Gd	10.5	8.4	8.4	7.0	4.1	6.0	5.3	4.4	6.0	5.5	6.7	6.4	7.9	4.7	5.6
Hf	5.1	4.6	5.8	3.7	4.5	4.8	4.0	6.0	5.0	4.7	4.3	5.1	4.2	3.5	3.2
Ho	1.8	1.5	1.4	1.2	0.7	1.0	0.9	0.9	1.0	0.9	1.2	1.1	1.4	0.9	0.9
La	61.3	51	47	38	23	31	31	25	32	30	36	37	44	27	31
Lu	0.7	0.6	0.6	0.5	0.3	0.4	0.4	0.3	0.4	0.4	0.5	0.4	0.6	0.3	0.4
Nb	32.0	30	30	21	25	26	25	32	28	24	24	27	26	19	19
Nd	61	48	45	37	22	31	30	24	31	29	36	36	43	26	29
Rb	39	43	49	52	56	44	60	56	47	57	64	54	55	41	42
Sc	18	19	22	15	14	18	15	18	21	18	20	17	17	16	13
Sm	12.9	10.3	9.6	7.7	4.4	6.4	6.0	4.9	6.6	6.2	7.5	7.4	8.8	5.4	6.0
Sr	645	516	410	778	356	536	449	169	372	259	211	129	284	197	397
Tb	1.7	1.3	1.4	1.1	0.6	0.9	0.8	0.7	0.9	0.8	1.1	1.0	1.2	0.8	0.9
Th	6.9	6.4	6.4	5.7	3.8	5.2	5.5	5.6	5.2	5.3	6.1	6.0	8.3	4.6	5.3
Tm	0.7	0.6	0.6	0.4	0.3	0.4	0.3	0.4	0.4	0.4	0.5	0.5	0.6	0.3	0.4
U	1.3	2.3	1.4	2.1	1.0	1.0	2.5	1.7	2.2	1.4	1.3	1.9	2.3	3.3	4.4
V	165	145	160	103	97	121	142	302	108	146	117	145	104	120	101
Yb	4.4	3.8	3.6	3.1	1.9	2.7	2.3	2.3	2.7	2.4	2.9	3.0	3.8	2.2	2.4
Zr	187	179	214	150	190	208	162	278	208	208	198	200	182	161	131
CIA	40	43	59	32	43	40	45	50	42	48	49	54	42	44	28
Eu*	0.78	0.78	0.81	0.70	0.72	0.74	0.72	0.69	0.71	0.70	0.69	0.70	0.69	0.68	0.70

†*Given in wt. %; Eu/Eu* = (2Eu/Eu$_{chondrite}$)/(Sm/Sm$_{chondrite}$ + Gd/Gd$_{chondrite}$).*

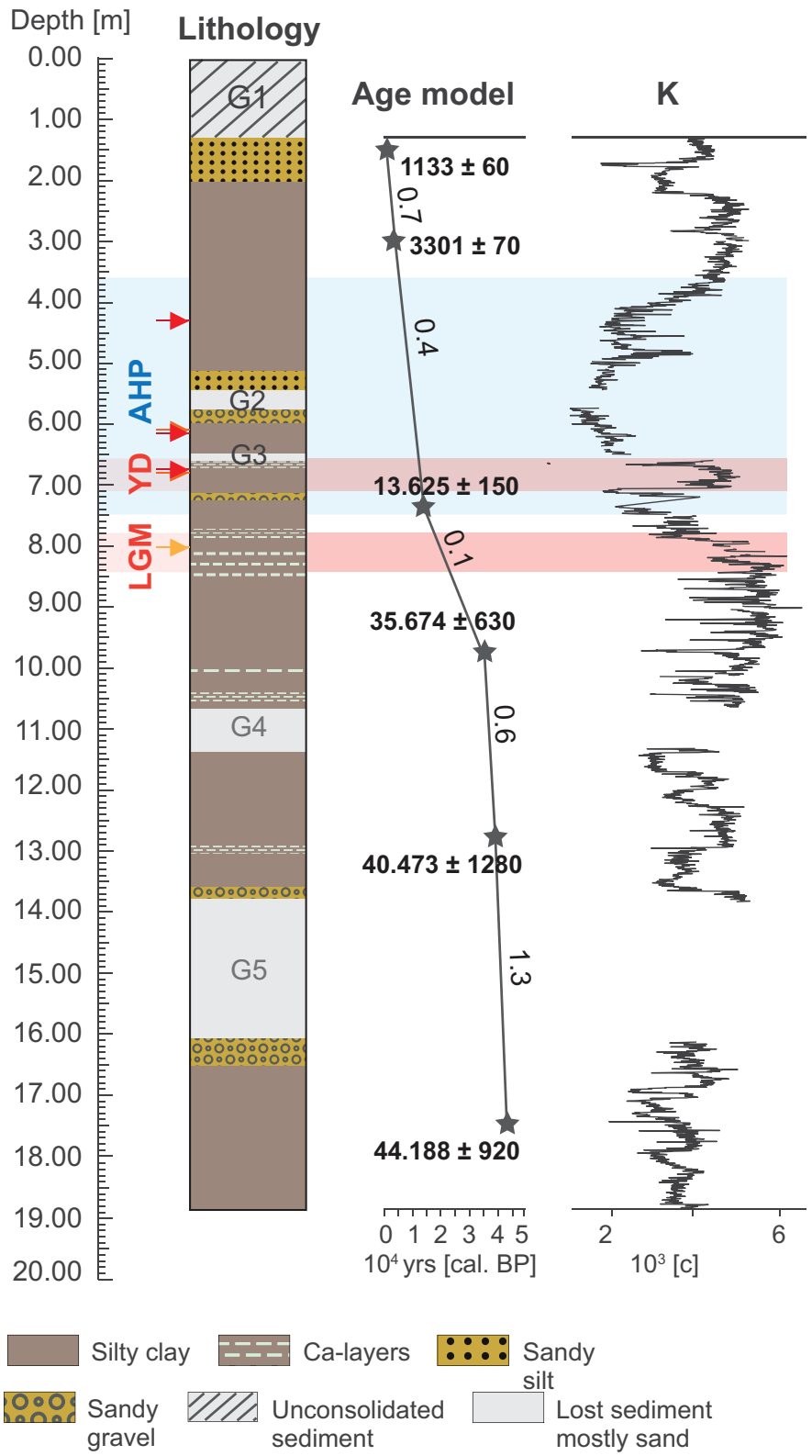

FIGURE 3 | Core lithology, age-depth model, and the Chew Bahir K record over the past ~45 kyrs.

Dryas (YD; ∼12.9–11.7 ka BP; Roberts et al., 1993) and Late Holocene (representing the last ∼2 ka BP of the record; **Figure 3**). Three samples (i.e., W4, W25, and W26) were collected in November 2018 for grain size analysis (**Figure 1**). W25 and W26 were collected from the Weyto River catchment entering into the Chew Bahir basin. W26 was collected from a freshly accumulated riverbank, while W25 represents an alluvial fan accumulation site between Weyto town and Weyto River. W4 was collected from a deep incised river at the foot of the Hammar range in the southern part of the Chew Bahir basin (see **Figure 1** for sample locations).

X-Ray Diffraction, Electron Microprobe and Grain Size Analysis

The mineralogical composition of powdered bulk sediments and oriented mounts of clay particles (<2 μm) were analyzed using X–ray powder diffraction (XRD) at the Department of Geosciences, Georgia State University. The clay fractions were extracted according to Stokes' settling velocity principle in 1,000 ml glassware. Randomly-oriented, powdered bulk samples were analyzed using Cu-Kα radiation (45 kV, 40 mA) from 5 to 70° 2θ, with a 0.02° 2θ step and 60 s per step, to identify a suite of non-clay minerals. Preferred-oriented samples of the <2 μm size fraction were analyzed in both air-dried (AD) and ethylene glycol-solvated (EG) states from 3 to 35° 2θ with a 0.02° 2θ step at 60 s per step, following the principles of Moore and Reynolds (1997).

The octahedral cation ratios [(Mg/(Al + Fe)] of the <0.1 μm size-fractions were determined using the JEOL-8200 electron microprobe at Rutgers University. The analyses were performed at 15 Kv accelerating voltage and 15 mA beam current, using a suite of in-house standards, including several hydroxyl-bearing sheet silicates, and derived from multiple sources. Data corrections were done using ZAF procedures. Since the samples are intrinsically fine-grained powders, normal polishing procedures could not be used and instead the samples had the form of compressed pellets that were sufficiently smooth to permit analysis. The presence of unquantified inter-grain voids reduces the overall density of the samples and, together with unanalyzed hydroxyl fractions, prevents the analysis totals reaching the nominal 100%.

Grain size analysis was carried out at the laboratory of the Geographic Institute, University of Cologne. Analysis was conducted in 116 channels from 0.04 to 2,000 mm with a Laser Diffraction Particle Size Analyzer (LS 13320 Beckmann CoulterTM), using the Fraunhofer optical model. Before analysis, organic and carbonate content was removed using 15% H2O2 and 10% HCL, respectively. Grain-size parameters are based on Folk and Ward (1957) and were calculated by GRADISTAT software version 8 (Blott and Pye, 2001).

Quantitative Multi-Element and Oxygen-Isotope Analysis

A total of 46 samples were analyzed for major, minor and trace elements at the Activation Laboratories Ltd. in Ontario, Canada following the analytical procedure termed "Code 4LITHO Major Elements Fusion ICP (WRA)/Trace Elements Fusion ICP/MS." Major, minor and trace element data were acquired by ICP-OES fusion and ICP-MS, respectively. Samples were analyzed in a batch system with each batch containing a method reagent blank, certified reference material and duplicates. Samples were analyzed for major oxides and selected trace elements (Code 4B) using Perkin Elmer Sciex ELAN 6000, 6100, or 9000 ICP/MS, providing a precision of ±5% and 10% for major and minor oxides, and trace elements at 100x the detection limit, respectively. Seven USGS and CANMET certified reference materials were used for calibration and one of the 7 standards was analyzed for every group of 10 samples. Three blanks and duplicates were analyzed per group of samples and every 15 samples, respectively.

The chemical index of alteration (CIA) was calculated on the basis of major element chemistry following Nesbitt and Young (1982) as follows:

$$CIA = [Al_2O_3/(Al_2O_3 + Na_2O + K_2O + CaO)] \times 100 \quad (1)$$

Six samples (3 each from DI and WI) were selected for clay mineral purification and subsequent oxygen-isotope analysis. Ultrafine clay size-fractions (<0.1 μm) were separated from the bulk sediments following routine centrifugation protocols (Moore and Reynolds, 1997) for XRD analysis. Samples were analyzed in both AD and EG states from 3 to 35° 2θ. Oxygen-isotope analyses were performed on the same samples at the Laboratory for Stable Isotope Science at the University *of* Western Ontario following Libbey et al. (2013) and references therein. The results are presented in the normal δ-notation relative to the VSMOW-SLAP calibrated scale in parts per thousand (‰). Reproducibility was better than ±0.2‰. VSMOW-SLAP calibrated standards analyzed as unknowns returned $\delta^{18}O$ = + 11.54 ± 0.2‰ (quartz; n = 2) and +10.18 ± 0.01‰ (carbon dioxide; n = 2), which compares well with their accepted values of +11.5‰ and +10.25‰, respectively (Huggett et al., 2017).

Geochemical Modeling

Geochemist's Workbench® (Bethke et al., 2019) was used to model the evaporative concentration of water with a dissolved solid composition equivalent to Lake Chamo, a freshwater lake that drains through the Segen River to the Chew Bahir basin (**Table 2**; Ayenew, 2005). Equilibrium reactions were modeled iteratively to dryness, assuming equilibrium gas exchange with the atmosphere. Equilibrium precipitation-dissolution was assumed with respect to gibbsite, and the precipitation of dolomite, talc, chrysotile, and mica were all suppressed as reaction kinetics likely do not favor these authigenic phases (Deocampo, 2010; Deocampo and Jones, 2014).

RESULTS

Mineralogy and Grain Size Distribution

The mineralogical assemblage of the WS samples is composed primarily of sand- and silt-size particles containing a higher fraction of non-clay mineral silicate phases than the MF samples,

TABLE 2 | Chemical composition of Lake Chamo water used for geochemical modeling.

Solute	Concentration (mg/L)
Na	265
K	14.1
Ca	2.2
Mg	3.8
Cl	64.9
SO_4	4.1
HCO_3	573
pH = 8.9	

which comprised mostly clay minerals. In addition to illite, smectite, and kaolinite, the <2 μm size-fraction of the WS samples also contain quartz and feldspar, and trace amounts of calcite and analcime (**Figure 4**). Analcime content increases in the MF samples that are transitional to the desiccated lake floor of the Chew Bahir basin. The <2 μm size-fraction of the MF samples contains illite, smectite and kaolinite (**Figure 4**).

Grain-size data of three samples are shown in **Supplementary Figure 2**. Two of the three samples (i.e., W26 and W4) show unimodal features, while one (W25) shows multimodal features (**Supplementary Figure 2**). All samples contained relatively little material in the 2–50 μm aeolian size range (**Supplementary Figure 2**). The amount of material within the 2–50 μm fraction in W26 and W4, and W25 samples is ∼14% and 36.8%, respectively.

Whole-Rock and Authigenic Clay Mineral Geochemistry

Major and trace element concentrations of the different sample groups show clear intergroup differences in the enrichment and depletion of certain major elements (**Table 1**). WS samples have higher SiO_2 (50–70 wt.%) contents compared to the MF samples (**Figure 5** and **Table 1**). In WS samples, as SiO_2 content increases, most other element abundances decrease, suggesting their association with non-quartz minerals. K_2O contents, however, remain relatively constant as SiO_2 varies. In MF samples, major element contents increase with increasing SiO_2, except for CaO, which strongly decreases. On the A–CN–K diagram (**Figure 6a**), WS samples are richest in Al_2O_3 (∼50–70%); CaO + Na_2O contents in MF samples trend toward the cluster of WS samples while their K_2O contents remain at ≤10%. On the A–CNK–FM diagram (**Figure 6b**), the CaO + Na_2O + K_2O content of some MF samples increases to ∼50% approaching the cluster of WS samples. CIA values (**Table 1**) range between 24 and 62 with WS samples consistently yielding higher values. Mean CIA values for WS and MF samples are 59 and 40, respectively. Mean CIA values for WI and DI samples are 44 and 42, respectively.

Upper Continental Crust-normalized (McLennan, 2001) chemical compositions of the sediments show that MF samples, on average, are enriched in elements such as Mg, Ca, Ce, Nd, and Na, and depleted of elements such as Ba and Zr relative to WS samples (**Figures 7a,b**). DI samples, on average, are enriched in Mg and depleted of K relative to WS samples (**Figures 7c,d**). Chondrite-normalized REE patterns reveal minor differences between the WS and MF samples (**Figure 8**). WS samples [e.g., mean $(La/Sm)_N$ = 2.61] are slightly depleted of Light REE (LREE) compared to MF samples [e.g., mean $(La/Sm)_N$ = 3.07] (**Figure 8**). Similarly, no significant differences are observed between Heavy REE (HREE) in WS [e.g., average $(Gd/Yb)_N$ = 1.61] and MF [e.g., average $(Gd/Yb)_N$ = 1.86] samples. No preferential removal of LREE or HREE is observed for either DI or WI samples (**Figure 8**). Eu anomalies in WS (mean Eu/Eu* = 0.85), MF (mean Eu/Eu* = 0.78), DI (mean Eu/Eu* = of 0.71), and WI (mean Eu/Eu* = 0.69) samples are also virtually identical (**Table 1**).

Whole-rock Ba/Sr ratios, a widely used proxy for weathering intensity (e.g., Buggle et al., 2011), show WS and WI samples generally having higher Ba/Sr ratios compared to MF and DI samples (**Figure 9a**). On average, MF samples have higher MgO/Al_2O_3 ratios (mean = 0.3) than WS samples (mean = 0.15), but both DI and WI samples have higher MgO/Al_2O_3 ratios compared to MF samples (**Figures 9a,b**). MgO/Al_2O_3 and Ba/Sr ratios in WS and MF samples show a somewhat higher degree of correlation (R^2 = 0.64) than in WI and DI samples (R^2 = 0.52; **Figure 9a**). MgO/Al_2O_3 and K_2O/Al_2O_3 ratios in DI and WI samples similarly show a high degree of correlation (R^2 = 0.64; **Figure 10a**), and this relationship is the same for MgO and K_2O.

Oxygen-isotope measurements of authigenic clay minerals ($\delta^{18}O_{illite-smectite}$ = + 22.44 to + 25.32‰) show that, except for one sample, the DI samples have higher $\delta^{18}O_{illite-smectite}$ compared to WI samples (**Figures 10b,c** and **Table 3**). The oxygen-isotope results for the <0.1 μm size-fraction also correlate well with the octahedral Mg/(Al + Fe) ratios determined by electron microprobe analysis (**Figure 10b** and **Table 3**).

Geochemical Modeling

Model results (**Figure 11**) show the immediate precipitation of calcite, reflecting the near-saturation of most surface waters in the region with respect to calcium carbonate. Evaporative concentration increases the amount of calcite precipitation and is also associated with analcime formation (Foerster et al., 2018). The next phase to reach supersaturation in the system is analcime ($NaAlSi_2O_6 \bullet H_2O$). Although solid phase analcime is stable in these surface waters, only a small mass of mineral was predicted to precipitate. The final phase to reach supersaturation is sepiolite [$Mg_4(Si_6O_{15})(OH)_2 \bullet 6H_2O$].

DISCUSSION

Weathering, Early Diagenesis and Authigenesis in Chew Bahir Sediments

The sedimentary deposits comprised in the Chew Bahir cores are primarily derived from Precambrian metamorphic rocks of the Hammar Range and the volcanic rocks at the northern and northeastern parts of the catchment via erosion and physical weathering of the source rock, which also facilitates chemical weathering. The CIA, first introduced by Nesbitt and Young (1982), has proved useful for quantifying progressive chemical weathering of the source rock, with higher

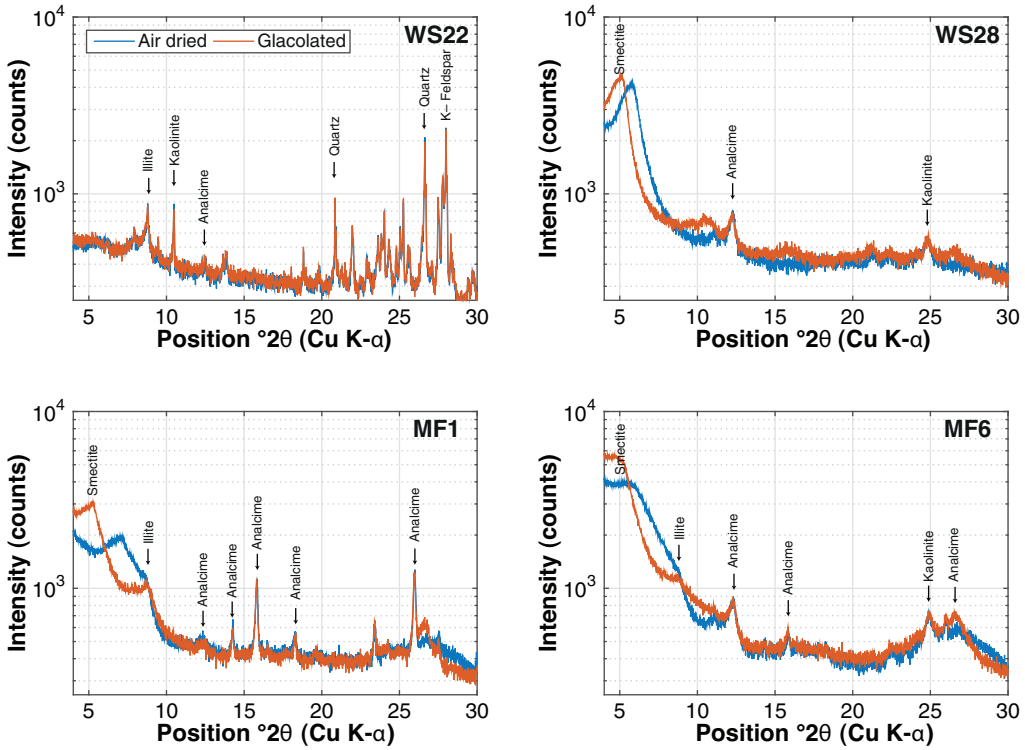

FIGURE 4 | XRD patterns of preferred-oriented, air-dried and glycolated mounts of the <2 μm size-fraction for four (4) WS and MF samples of modern Chew Bahir sediments. WS, modern watershed; and MF, modern mudflat. XRD patterns for air-dried samples are shown in blue, and those for samples treated with ethylene glycol, red.

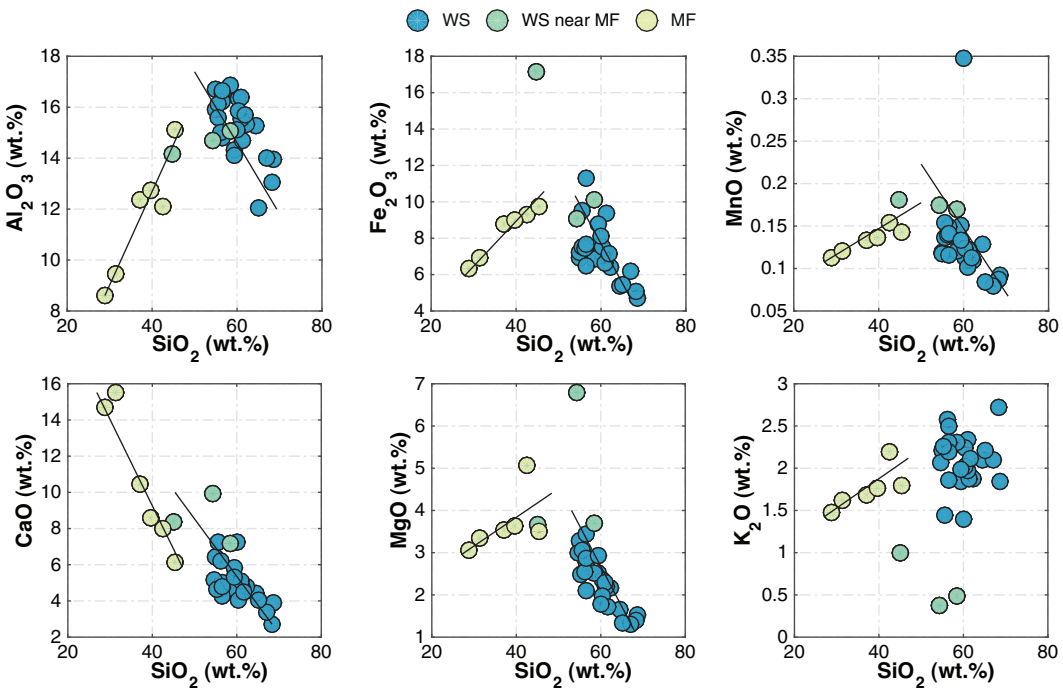

FIGURE 5 | Relationships between major element oxide and SiO_2 contents in WS and MF samples. WS, modern watershed; and MF, modern mudflat.

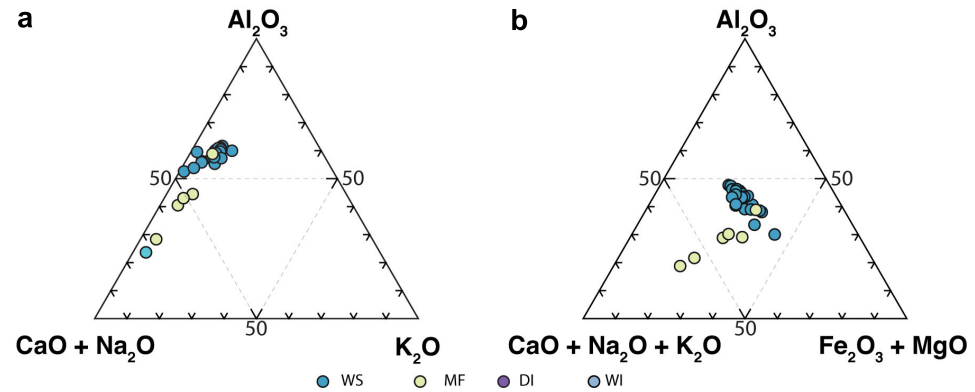

FIGURE 6 | Ternary plots of **(a)** A-CN-K, and **(b)** A-CNK-FM illustrating the degree of alteration in WS, MF, WI, and DI samples. WS, modern watershed sample; and MF, modern mudflat sample.

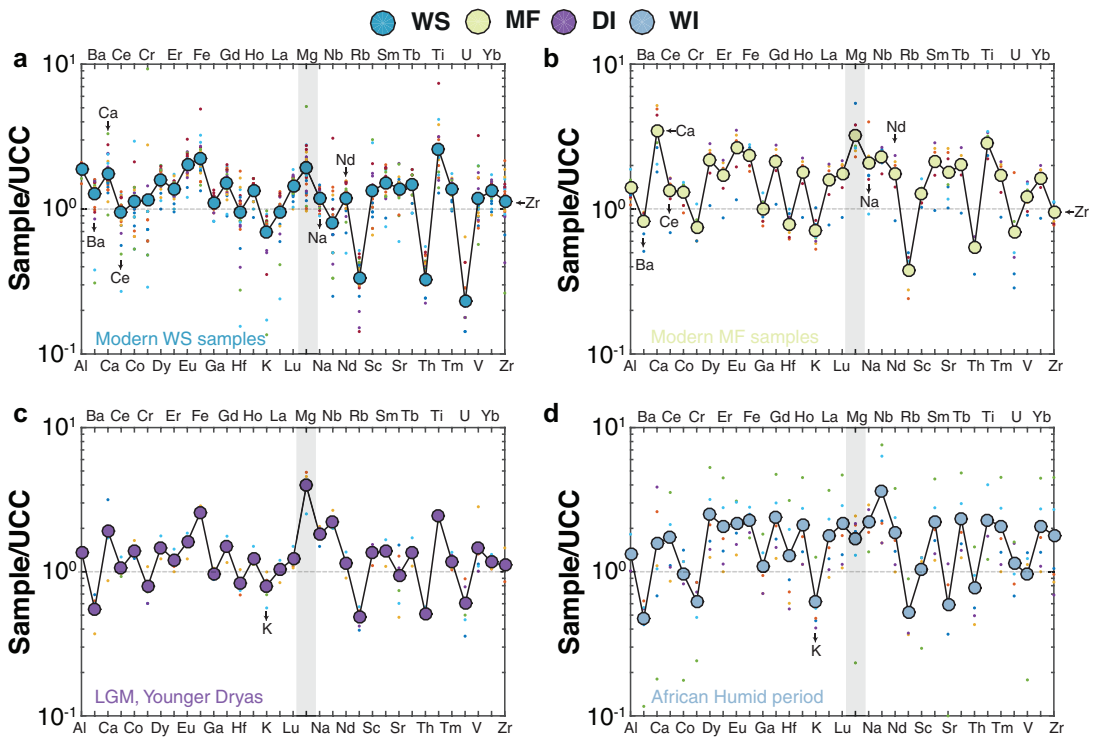

FIGURE 7 | Upper Continental Crust (UCC)-normalized (McLennan, 2001) chemical composition in **(a)** WS, **(b)** MF, **(c)** DI, and **(d)** WI samples. Colored dots show the individual averages for each sample group. WS, modern watershed; MF, modern mudflat; MF, modern mudflat; DI, late Quaternary dry interval; and WI, late Quaternary wet interval.

values indicating stronger weathering. In the case of WS samples, both physical weathering of the source rock material (i.e., metamorphosed granitic and gneissic rocks) and progressive chemical weathering are likely at play. The presence of authigenic carbonates, abundant in MF samples, however, complicates application of the CIA when endeavoring to capture the true extent of weathering (e.g., Cullers, 2000; Buggle et al., 2011; Garzanti et al., 2014). The Fe_2O_3, MnO, and K_2O contents of both WS and MF samples are about the same but the CaO content is generally higher in MF samples (**Figure 5**). Solving Equation 1 excluding CaO provides higher CIA values for WS samples (i.e., mean CIA = 74) than MF samples (i.e., mean CIA = 60), indicating stronger weathering in WS samples than MF samples. Although the unavailability of a systematic dust record is a key limitation, the conclusion that sedimentary deposits comprised in the Chew Bahir cores are primarily derived from Precambrian metamorphic rocks of the Hammar Ranis is consistent with the inferences made from XRD and grain size data (**Supplementary Figures 1**, **2**). The XRD data do not show evidence for windblown or distant aeolian-transported

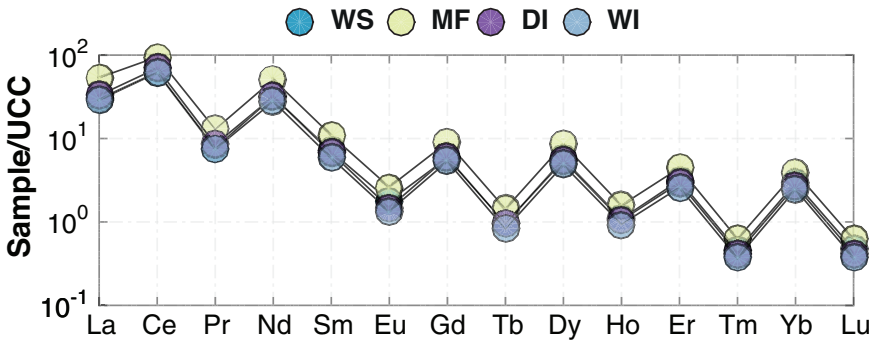

FIGURE 8 | REE patterns normalized to chondrite (McDonough and Sun, 1995) in MF (yellow-green), DI (purple), WI (light blue), and WS (blue) samples. WS, modern watershed; MF, modern mudflat; DI, late Quaternary dry interval; and WI, late Quaternary wet interval.

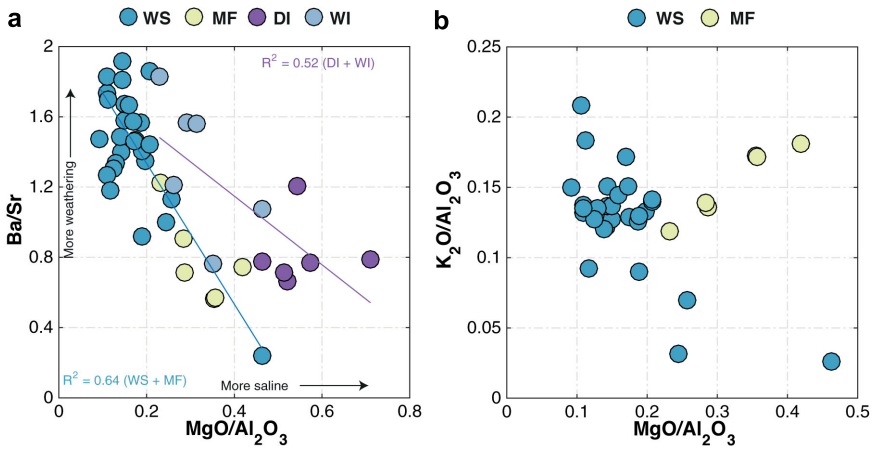

FIGURE 9 | Comparison between **(a)** Ba/Sr and MgO/Al_2O_3 for WS, MF, DI, and WI samples and **(b)** K_2O/Al_2O_3 and MgO/Al_2O_3 for WS and MF samples. WS, modern watershed; MF, modern mudflat; DI, late Quaternary dry interval; and WI, late Quaternary wet interval. The R^2 values shown in the lower left corner of **(b)** are for Ba/Sr versus MgO/Al_2O_3 in WS and MF (blue), and WI and DI (purple) samples, respectively. Arrows in **(b)** show direction of increase in weathering intensity and salinity inferred from the Ba/Sr and MgO/Al_2O_3 ratios, respectively.

dust sources, which are commonly associated with clay minerals such as palygorskite (see, for example, Ehrmann et al., 2017 and **Supplementary Figure 1**). Two of the three samples (i.e., W26 and W4) collected for grain size analysis derived from freshly transported material of recent riverbeds show unimodal features and very little material in the 2–50 μm aeolian size range (**Supplementary Figure 2**). W25 collected from an alluvial fan accumulation is a mixture of different grain-size fractions with multimodal features, suggesting strong local fluvial reworking (**Supplementary Figure 2**). The amount of material in the 2–50 μm size range is also much higher in W25 (∼36. 8%) than in W26 and W4 (∼14.4%), and lends further support for the aforementioned interpretations vis-à-vis the source of Chew Bahir sediments. We concede, however, that the above interpretations need to be independently verified using dust traps.

As described in the Results section, notable differences in major and minor whole-rock geochemistry exist between MF and WS samples (**Figure 5** and **Table 1**). Differences also include significant enrichment of MF samples compared to WS samples in some mobile elements (e.g., Na and Mg), which may have been introduced externally from saline, alkaline pore waters (**Figures 7a,b**). Na contents in WI and DI samples, however, are not significantly different (**Figure 7c,d**). The decreasing trend in Al_2O_3, Fe_2O_3, MnO, and MgO contents with increasing SiO_2 in the WS samples reflects the process involved in the formation of the source granitic rocks by a simple fractional crystallization (e.g., Asrat and Barbey, 2003). However, the MF samples also show an increase in MgO, which indicates its possible enrichement during chemical weathering (e.g., clay formation; **Figure 5**).

The true extent of early diagenetic control on the elemental composition of Chew Bahir sediments is amplified in their clay mineralogy. The modern MF samples mostly contain illite, Mg-rich smectite and some kaolinite (**Figure 4**). The Mg enrichment observed in clay minerals from MF samples is similar to late Quaternary DI samples and most likely reflects authigenic clay mineral formation from the alteration of feldspathic glass

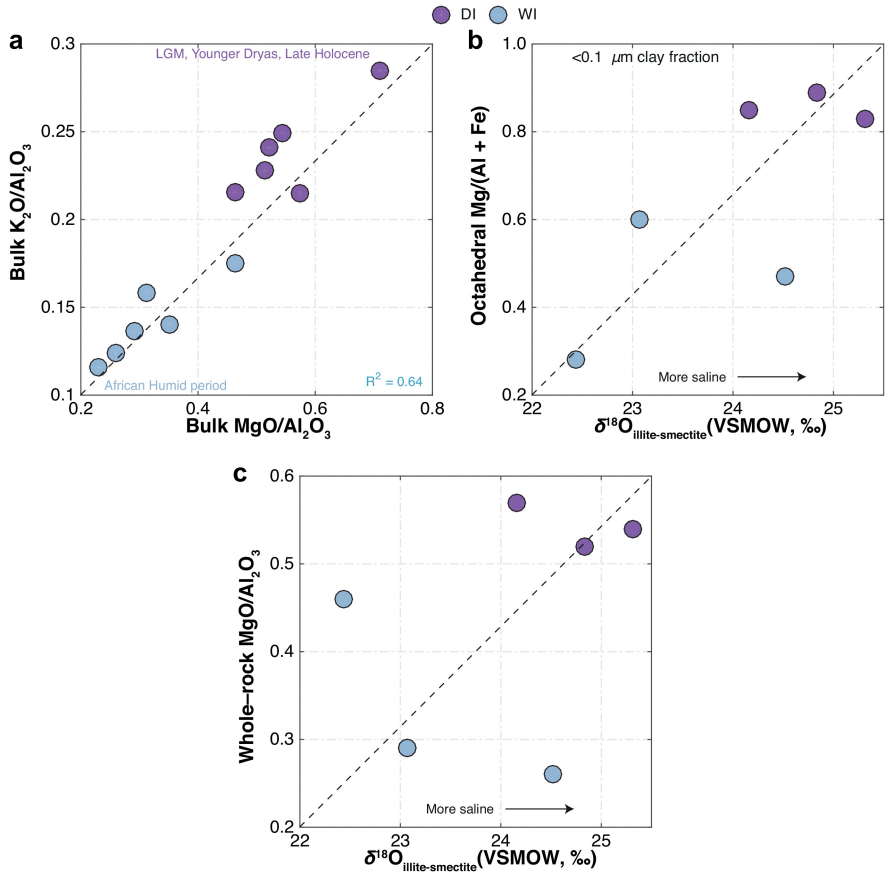

FIGURE 10 | Comparison for DI and WI samples between **(a)** bulk K_2O/Al_2O_3 and MgO/Al_2O_3, **(b)** octahedral Mg/(Al + Fe) versus $\delta^{18}O$ of authigenic illite-smectite (<0.1 μm size-fraction), and **(c)** bulk MgO/Al_2O_3 versus $\delta^{18}O$ of authigenic illite-smectite (<0.1 μm size-fraction). Arrows in **(b,c)** show direction of increase in salinity deduced from $\delta^{18}O_{illite-smectite}$.

TABLE 3 | $\delta^{18}O$ values and octahedral cation ratios for illite-smectite from late Quaternary samples.

Samples	Timing (Sample group)	$\delta^{18}O_{illite-smectite}$ (‰)*	Oct Mg	Oct Fe	Oct Al	Oct Mg/(Fe + Al)*
CB- 05- 2010- 478	LGM (DI)	+25.32	0.44	0.73	0.81	0.87
CB- 01- 2009-658	AHP (WI)	+23.07	0.80	0.64	0.68	0.65
CB- 03- 2010- 468	AHP (WI)	+24.52	0.99	0.75	0.46	0.47
CB- 01- 2009-730	YD (DI)	+24.83	1.06	0.74	0.46	0.95
CB- 03- 2010- 570	YD (DI)	+24.16	0.98	0.79	0.37	1.08
CB- 01- 2009- 450	AHP (WI)	+22.44	0.64	0.59	0.76	0.32

*<0.1 μm size-fraction.

(Deocampo and Jones, 2014; Deocampo, 2015), a precursor phase present in abundant quantities in the Chew Bahir basin (Foerster et al., 2018).

Watershed samples also show a slightly higher degree of LREE and HREE fractionation compared to MF samples, while all sample groups also have negative Eu anomalies with no clear differences between WS and MF samples (average Eu/Eu* of 0.85 versus 0.78, respectively; **Table 1**) or WI and DI samples (average Eu/Eu* of 0.71 versus 0.69, respectively; **Table 1**). Assuming Eu concentration is not affected by weathering, a negative Eu anomaly is an indication of strong plagioclase fractionation in the source rocks; notably, the Proterozoic granitic and gneissic rocks of the Hammar Range show strong negative Eu anomalies (Asrat and Barbey, 2003). It also suggests that the bulk sediment source rock remained very similar through time. In short, the REE data suggest that the detrital sediment load is predominantly derived from the Hammar Range.

Consistent with the CIA, intergroup comparisons between MgO/Al_2O_3 and K_2O/Al_2O_3 or Ba/Sr for the bulk sediments suggest that the intensity of weathering, inferred from Ba/Sr data, is (and was) highest in late Quaternary WI and modern WS samples (**Figure 9a**). Although the link between weathering

and geochemical proxy formation is known to be more complex, Ba/Sr ratios are routinely used as a weathering proxy. The power of this proxy is provided by the selective removal of more mobile Sr coupled with the relative immobility of Ba, which is readily adsorbed by clay minerals during weathering (e.g., Nesbitt and Markovics, 1980; Middelburg et al., 1988; Deocampo et al., 2010). By comparison, DI samples have consistently higher MgO/Al_2O_3, while $K_2O/Al2O_3$ in MF samples holds constant (**Figure 10b**). A strong positive relationship between MgO/Al_2O_3 and K_2O/Al_2O_3 (also between MgO and K_2O) within the mudflat samples indicates the effect of greater exposure to salinity and alkalinity on the mudflats, with octahedral Mg substitution and K-uptake due to incipient illitization (Deocampo, 2015; **Figure 9b**). The presence of both smectite and illite-smectite (the latter formed by low temperature illitization of smectite; e.g., Eberl et al., 1986) is reminiscent of similar differences observed between the late Quaternary WI and DI samples. The geochemistry of MF samples is most likely constrained by diagenesis and authigenic mineral formation, rather than solely representing the end product of weathering. Indeed, neoformation of clay minerals in alkaline solutions is termed "inverse weathering" as it is chemically the opposite of silicate hydrolysis, which produces authigenic alkaline silicate minerals (Deocampo and Jones, 2014; Deocampo, 2015).

The presence of analcime, a precursor zeolite formed under conditions of increasing lake water salinity and alkalinity, is noteworthy in all MF samples and WS samples collected near the desiccated lake floor (**Figure 4**). Analcime is also present in cores collected from the center of the Chew Bahir basin (e.g., Viehberg et al., 2018). Analcime can form under diverse physical, chemical and geological settings including marine and hydrothermal alteration, but it is much more common in saline and alkaline lake deposits (e.g., Hay and Sheppard, 2001). We have considered a range of possibilities to explain diagenetic formation of analcime in the Chew Bahir basin. In some other eastern African lakes such as Lake Magadi, analcime is thought to form by reaction of precursor zeolites, volcanic glass, hydrous sodium aluminosilicate gels or a combination of all three phases in saline alkaline solutions (e.g., Surdam and Eugster, 1976). In other eastern African rift lakes such as Lake Bogoria, authigenic analcime has been shown to form from poorly crystalline smectite clay minerals reacting with saline, alkaline pore fluids (e.g., Renaut, 1993).

Hydrogeochemical Processes in the Chew Bahir Basin

The Geochemist's Workbench[§] model results indicate that evaporative concentration increases the amount of calcite precipitation, eventually eliminating calcium from evolved waters (Deocampo and Jones, 2014). The next phase to reach supersaturation in the model system is analcime ($NaAlSi_2O_6 \bullet H_2O$; **Figure 11**). This reflects the high alkalinity of the waters in the presence of reactive aluminosilicates (Hay, 1978). Although analcime is stable in these modeled waters, however, only a small mass of mineral was predicted to precipitate. This suggests that the significant accumulations of analcime observed in the Chew Bahir sediments (e.g., Foerster et al., 2018) result not only from evaporative concentration, but also from alteration of locally abundant volcanic glass in alkaline waters (Hay and Sheppard, 2001).

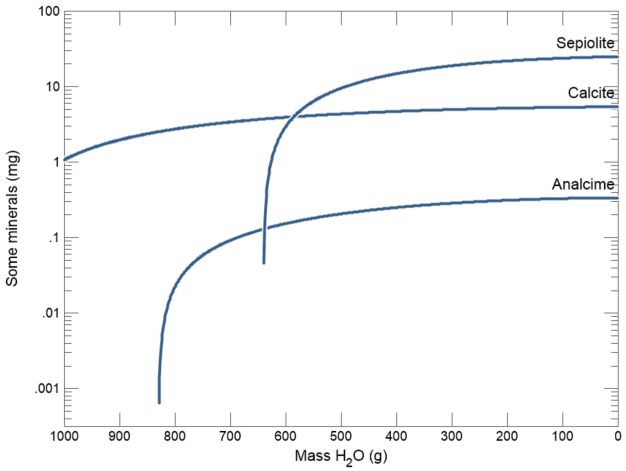

FIGURE 11 | Modeled hydrochemical evolution and mineral reaction pathways in the Chew Bahir basin showing the immediate precipitation of calcite, and followed by analcime and sepiolite, calculated based on Lake Chamo dissolved solid composition (**Table 2**; Ayenew, 2005).

Sepiolite [$Mg_4(Si_6O_{15})(OH)_2 \bullet 6H_2O$] is the final phase to reach supersaturation in the modeled system (**Figure 11**). Although sepiolite has not been observed locally and is not expected to precipitate in this setting, we can use its thermodynamics to model the behavior of Mg-silicates more generally (Deocampo, 2005, 2015). Abundant aluminous detrital clay minerals in fluvio-lacustrine environments provide reactive substrates with low kinetic barriers for precipitation of Mg-rich interstratifications rather than pure Mg-silicate such as sepiolite (Deocampo, 2015). The model prediction of sepiolite precipitation shows the potential for Mg-rich authigenic clay minerals to form, which is well known as an indicator of elevated salinity in lake deposits in the region (Deocampo et al., 2017; Foerster et al., 2018).

In sum, thermodynamic modeling of evaporating Lake Chamo water produces an authigenic mineral assemblage typical of both modern lake mudflats in the Chew Bahir basin and Late Quaternary sediments recovered from cores (Foerster et al., 2018). These data suggest that the mineral assemblage of calcite, analcime, and Mg-enriched authigenic illitic clay minerals is indicative of environments of enhanced evaporative concentration in the basin.

Refining Interpretation of the Chew Bahir K Record Using Whole-Rock and Clay Mineral Geochemistry

Foerster et al. (2018) demonstrated that K content in the Chew Bahir sediments is likely derived from enhanced K-fixation during dry high-salinity episodes. Salinity in the hydrologically closed paleo-Lake Chew Bahir was controlled by the amount of

TABLE 4 | Arid and humid phases identified based on multi-proxy indicators.

Chew Bahir proxies	Arid	Humid
K concentration (counts)	↑	↓
Clay mineralogy (Illite versus smectite)	Illite ↑	Smectite ↑
Zeolite mineralogy	Analcime ↑	Analcime ↓
Oxygen isotopes	↑	↓
Ba/Sr ratios	↓	↑

paleo-precipitation in the catchment and the rate of evaporation in the paleolake. It is therefore conceivable that the chemical composition of the paleolake significantly impacted the crystal chemistry of authigenic minerals present in the sediment, including the progress of K-fixation in clay minerals (Foerster et al., 2018). Like many other eastern African rift lakes, aridity and the prevalence of hypersaline conditions facilitate authigenic illitization of smectite (e.g., Singer and Stoffers, 1980; Deocampo et al., 2009) and consequently K-enrichment in Chew Bahir sediments. The major element geochemistry of the late Quaternary DI and WI samples establishes a clear relationship between K-enrichment in Chew Bahir sediments and hypersaline conditions in the basin (**Figure 10a**). It should also be noted that sediments deposited during humid episodes (e.g., during the AHP) had whole-rock MgO/Al_2O_3 ratios ranging from ∼0.2 to 0.4, whereas those deposited during arid episodes (e.g., at LGM and YD times) had MgO/Al_2O_3 ratios ranging from ∼0.5 to 0.7, indicating higher salinity (**Figure 10a**). These results show that ancient sediments deposited during dry periods most similarly resemble modern saline mudflats in dry-Lake Chew Bahir today and had Ba/Sr values ranging from ∼0.6 to 1.2 (**Figure 9a**). Conversely, sediments deposited during relatively wetter periods, such as the AHP, have sources similar to those found presently in upstream locations, e.g., WS samples.

The proposed relationship between basin aridity and K uptake in the sediment is compared with oxygen-isotope analysis of authigenic illite-smectite. The oxygen−isotope composition of authigenic clay minerals formed in lake water at isotopic equilibrium is controlled primarily by clay mineral composition, structure, and water temperature (Savin and Lee, 1988). Once formed, oxygen in the tetrahedral and octahedral sheets does not undergo isotopic exchange with pore fluids in the absence of dissolution−precipitation reactions. In the current study, the $\delta^{18}O_{illite-smectite}$ has been determined by the oxygen-isotope composition of the incoming waters draining through the Weyto River (**Figures 1b,c**) and the extent of lake-water evaporation (e.g., Gebregiorgis et al., 2020a). Lake-water $\delta^{18}O$ is certainly influenced by the isotopic composition of the prevailing source (i.e., Lake Chamo; see **Figure 1b**) during periods of rapid lake level change. This signal, however, is likely overprinted in a system like Chew Bahir, where the extent of lake-water ^{18}O-enrichment was largely driven by evaporation.

The $\delta^{18}O$ of authigenic illite-smectite in the late Quaternary WI and DI samples range from +22.4 to +24.5‰ (average + 23.3‰), and +24.1 to +25.3‰ (average + 24.77‰), respectively (**Figures 10b,c**). Notably wet (i.e., during the AHP) and dry (e.g., at LGM and YD times) periods of the late Quaternary have been identified from the Chew Bahir K record, which are now largely confirmed independently by these oxygen-isotope measurements. The authigenic illite-smectite is generally most enriched in ^{18}O during periods of regional aridity, which also coincides with significant Mg enrichment (**Figure 10b** and **Table 3**) and low-temperature illitization suggestive of enhanced evaporative concentration in the basin (**Figure 11** and **Table 4**). Collectively, our results confirm that, in closed-basin lake deposits not overly diluted by detrital or biogenic sediments, subtle changes in water balance can be detected using both elemental and oxygen-isotope analysis of submicron authigenic clay minerals. Our first attempt to reproduce the climate signals recorded in the Chew Bahir K record using oxygen-isotope measurements of authigenic illite-smectite from notable warm/wet (e.g., during the Mid-Holocene) and cold/dry intervals (e.g., during the LGM) has proven to be successful.

CONCLUSION

New mineralogical and geochemical data from modern and ancient sediments in the Chew Bahir basin shed light on the role of sedimentary processes in chemical proxy formation. The data presented here show that the geochemistry of the modern saline mudflats in dry Lake Chew Bahir today resemble ancient sediments deposited during dry periods. Conversely, the geochemistry of modern detrital upstream sources can be compared to sediments deposited during relatively wetter periods, such as the AHP. This study demonstrates that interpretation of such geochemical datasets is complex and highly site-specific, and careful evaluation of any seemingly straightforward relationship between sediment composition and climate is required. This knowledge is critical for understanding proxy formation in playa sites and sedimentary records from semi-arid regions of the world.

DATA AVAILABILITY STATEMENT

All data generated or analyzed during this study are included in this published article.

AUTHOR CONTRIBUTIONS

DG, DD, VF, and AA designed the project. DD conducted the geochemical modeling. FL provided and acquired funding for the oxygen-isotope analyses. AA, FS, HL, and MT acquired the funding, designed, and directed the Chew Bahir Drilling Project as part of the Hominin Sites and Paleolakes Drilling Project, directed by A. Cohen of the University of Arizona. FS, AA, HL, and VF did the coring at Chew Bahir. JD carried out electron probe microanalyses of samples. VF, FS, AJ, MM, and HL added modern samples to this study. SO carried out grain size analysis of samples. DG led sample collection, data analysis, and wrote the manuscript with contributions from all co-authors. All authors revised the manuscript.

FUNDING

This research was supported by NSF grant (NSF 1349651) to DD. The oxygen-isotope measurements were supported by a Natural Sciences and Engineering Research Council Discovery Grant of Canada and the Canada Research Chairs Program (FL). FS acknowledges further funding from the DFG through grants SCHA 472/13 and SCHA 472/18. MT acknowledges funding from the DFG through grants TR 419/8, TR 419/9, and TR 419/16. In addition, FS acknowledges funding from the CRC 806 Research Project "Our way to Europe" – Project Number 57444011. HL was funded by grant NE/K014560/1 from the UK Natural Environment Research Council. This was Western's Laboratory for Stable Isotope Science Contribution #385.

SUPPLEMENTARY MATERIAL

The Supplementary Material for this article can be found online at: https://www.frontiersin.org/articles/10.3389/feart.2021.607695/full#supplementary-material

REFERENCES

Asrat, A., and Barbey, P. (2003). Petrology, geochronology and Sr–Nd isotopic geochemistry of the konso pluton, south-western ethiopia: implications for transition from convergence to extension in the mozambique belt. *Int. J. Earth Sci.* 92, 873–890. doi: 10.1007/s00531-003-0360-9

Ayenew, T. (2005). Major ions composition of the groundwater and surface water systems and their geological and geochemical controls in the ethiopian volcanic terrain. *SINET Ethiopian J. Sci.* 28, 171–188.

Bethke, C. M., Farrell, B., and Yeakel, S. (2019). *GWB essentials guide*. Champaign, Illinois: Aqueous Solutions, LLC.

Blott, S. J., and Pye, K. (2001). GRADISTAT: a grain size distribution and statistics package for the analysis of unconsolidated sediments. *Earth Surface Processes Landforms* 26, 1237–1248. doi: 10.1002/esp.261

Brown, E., Johnson, T., Scholz, C. A., Cohen, A., and King, J. (2007). Abrupt change in tropical african climate linked to the bipolar seesaw over the past 55,000 years. *Geophys. Res. Lett.* 34:20702. doi: 10.1029/2007GL031240

Buggle, B., Glaser, B., Hambach, U., Gerasimenko, N., and Marković, S. (2011). An evaluation of geochemical weathering indices in loess–paleosol studies. *Quaternary Int.* 240, 12–21. doi: 10.1016/j.quaint.2010.07.019

Burnett, A. P., Soreghan, M. J., Scholz, C. A., and Brown, E. T. (2011). Tropical east african climate change and its relation to global climate: a record from lake tanganyika, tropical east africa, over the past 90+ kyr. *Palaeogeogr. Palaeoclimatol. Palaeoecol.* 303, 155–167. doi: 10.1016/j.palaeo.2010.02.011

Chesworth, W., Dejou, J., and Larroque, P. (1981). The weathering of basalt and relative mobilities of the major elements at belbex, france. *Geochimica et Cosmochimica Acta* 45, 1235–1243. doi: 10.1016/0016-7037(81)90147-2

Clark, P. U., Dyke, A. S., Shakun, J. D., Carlson, A. E., Clark, J., Wohlfarth, B., et al. (2009). The last glacial maximum. *Science* 325, 710–714.

Clift, P. D., Wan, S., and Blusztajn, J. (2014). Reconstructing chemical weathering, physical erosion and monsoon intensity since 25 ma in the northern south china sea: a review of competing proxies. *Earth Sci. Rev.* 130, 86–102. doi: 10.1016/j.earscirev.2014.01.002

Croudace, I. W., Löwemark, L., Tjallingii, R., and Zolitschka, B. (2019). Current perspectives on the capabilities of high resolution XRF core scanners. *Quaternary Int.* 514, 5–15. doi: 10.1016/j.quaint.2019.04.002

Croudace, I. W., Rindby, A., and Rothwell, R. G. (2006). "ITRAX: description and evaluation of a new multi-function X-ray core scanner," in *New techniques in sediment core analysis*, ed. R. G. Rothwell (London, UK: Geological Society of London), 51–63.

Cullers, R. L. (2000). The geochemistry of shales, siltstones and sandstones of pennsylvanian–permian age, colorado, USA: implications for provenance and metamorphic studies. *Lithos* 51, 181–203. doi: 10.1016/S0024-4937(99)00063-8

Davidson, A. (1983). The omo river project: reconnaissance geology and geochemistry of parts of Ilubabor, kefa, gemu gofa and sidamo. *Ethiopian Instit. Geol. Surv. Bull.* 2, 1–89.

Demenocal, P., Ortiz, J., Guilderson, T., Adkins, J., Sarnthein, M., Baker, L., et al. (2000). Abrupt onset and termination of the african humid period: rapid climate responses to gradual insolation forcing. *Quaternary Sci. Rev.* 19, 347–361. doi: 10.1016/S0277-3791(99)00081-5

Deocampo, D., Cuadros, J., Wing-Dudek, T., Olives, J., and Amouric, M. (2009). Saline lake diagenesis as revealed by coupled mineralogy and geochemistry of multiple ultrafine clay phases: pliocene olduvai gorge, tanzania. *Am. J. Sci.* 309, 834–868. doi: 10.2475/09.2009.03

Deocampo, D. M. (2004). Authigenic clays in east africa: regional trends and paleolimnology at the plio–pleistocene boundary, olduvai gorge, tanzania. *J. Paleolimnol.* 31, 1–9. doi: 10.1023/B:JOPL.0000013353.86120.9b

Deocampo, D. M. (2005). Evaporative evolution of surface waters and the role of aqueous CO2 in magnesium silicate precipitation: lake eyasi and ngorongoro crater, northern tanzania. *South Afric. J. Geol.* 108, 493–504. doi: 10.2113/108.4.493

Deocampo, D. M. (2010). The geochemistry of continental carbonates. *Dev. Sedimentol.* 62, 1–59. doi: 10.1016/S0070-4571(09)06201-3

Deocampo, D. M. (2015). Authigenic clay minerals in lacustrine mudstones. *Geol. Soc. Am. Spl. Papers* 515, SE503–SE515.

Deocampo, D. M., Behrensmeyer, A. K., and Potts, R. (2010). Ultrafine clay minerals of the pleistocene olorgesailie formation, southern kenya rift: diagenesis and paleoenvironments of early hominins. *Clays Clay Minerals* 58, 294–310. doi: 10.1346/CCMN.2010.0580301

Deocampo, D. M., Berry, P. A., Beverly, E. J., Ashley, G. M., and Jarrett, R. E. (2017). Whole-rock geochemistry tracks precessional control of pleistocene lake salinity at olduvai gorge, tanzania: a record of authigenic clays. *Geology* 45, 683–686. doi: 10.1130/G38950.1

Deocampo, D. M., and Jones, B. F. (2014). "Geochemistry of saline lakes," in *Treatise on Geochemistry*, Second Edn, eds H. D. Holland and K. K. Turekian (Amsterdam: Elsevier), 437–469.

Deocampo, D. M., and Tactikos, J. C. (2010). Geochemical gradients and artifact mass densities on the lowermost Bed II eastern lake margin (˜ 1.8 Ma), olduvai gorge, tanzania. *Quaternary Res.* 74, 411–423. doi: 10.1016/j.yqres.2010.09.004

Eberl, D. D., Środoń, J., and Northrop, H. R. (1986). "Potassium fixation in smectite by wetting and drying," in *Geochemical Processes at Mineral Surfaces*, eds J. A. Davies and K. F. Hayes (Washington, DC: American Chemical Society Symposium), 296–326.

Ebinger, C., Yemane, T., Harding, D., Tesfaye, S., Kelley, S., and Rex, D. (2000). Rift deflection, migration, and propagation: linkage of the ethiopian and eastern rifts, africa. *Geol. Soc. Am. Bull.* 112, 163–176. doi: 10.1130/0016-76062000112<163:RDMAPL<2.0.CO;2

Ehrmann, W., Schmiedl, G., Beuscher, S., and Krüger, S. (2017). Intensity of african humid periods estimated from saharan dust fluxes. *PloS one* 12:e0170989. doi: 10.1371/journal.pone.0170989

Fischer, M. L., Markowska, M., Bachofer, F., Foerster, V. E., Asrat, A., Zielhofer, C., et al. (2020). Determining the pace and magnitude of lake level changes in southern ethiopia over the last 20,000 years using lake balance modelling and SEBAL. *Front. Earth Sci.* 8:197. doi: 10.3389/feart.2020.00197

Foerster, V., Deocampo, D. M., Asrat, A., Günter, C., Junginger, A., Krämer, K. H., et al. (2018). Towards an understanding of climate proxy formation in the chew bahir basin, southern ethiopian rift. *Palaeogeogr. Palaeoclimatol. Palaeoecol.* 501, 111–123. doi: 10.1016/j.palaeo.2018.04.009

Foerster, V., Junginger, A., Langkamp, O., Gebru, T., Asrat, A., Umer, M., et al. (2012). Climatic change recorded in the sediments of the chew bahir basin, southern ethiopia, during the last 45,000 years. *Quaternary Int.* 274, 25–37. doi: 10.1016/j.quaint.2012.06.028

Folk, R. L., and Ward, W. C. (1957). Brazos river bar: a study in the significance of grain size parameters. *J. Sediment. Petrol.* 27, 3–26. doi: 10.1306/74D70646-2B21-11D7-8648000102C1865D

Garzanti, E., Padoan, M., Setti, M., López-Galindo, A., and Villa, I. M. (2014). Provenance versus weathering control on the composition of tropical river mud (southern africa). *Chem. Geol.* 366, 61–74. doi: 10.1016/j.chemgeo.2013.12.016

Gebregiorgis, D., Deocampo, D. M., Longstaffe, F. J., Simpson, A., Ashley, G. M., Beverly, E. J., et al. (2020a). Oxygen isotopes in authigenic clay minerals: Toward building a reliable salinity proxy. *Geophys. Res. Lett.* 47:e2019GL085576. doi: 10.1029/2019GL085576

Gebregiorgis, D., Giosan, L., Hathorne, E. C., Anand, P., Nilsson-Kerr, K., Plass, A., et al. (2020b). What can we learn from X-ray fluorescence core scanning data? A paleomonsoon case study. *Geochem. Geophys. Geosyst.* 21:e2019GC008414. doi: 10.1029/2019GC008414

Gebregiorgis, D., Rayner, D., and Linderholm, H. W. (2019). Does the IOD independently influence seasonal monsoon patterns in northern ethiopia? *Atmosphere* 10:432. doi: 10.3390/atmos10080432

Harriss, R. C., and Adams, J. A. (1966). Geochemical and mineralogical studies on the weathering of granitic rocks. *Am. J. Sci.* 264, 146–173. doi: 10.2475/ajs.264.2.146

Hay, R. L. (1978). "Geologic occurrence of zeolites," in *Natural zeolites: Occurrence, properties, use*, eds L. B. Sand and F. A. Mumpton (Elmsford, NY: Pergamon Press), 135–143.

Hay, R. L., and Sheppard, R. A. (2001). Occurrence of zeolites in sedimentary rocks: an overview. *Rev. Mineral. Geochem.* 45, 217–234. doi: 10.2138/rmg.2001.45.6

Hendy, I. L., Napier, T. J., and Schimmelmann, A. (2015). From extreme rainfall to drought: 250 years of annually resolved sediment deposition in santa barbara basin, california. *Quaternary Int.* 387, 3–12. doi: 10.1016/j.quaint.2015.01.026

Hession, S. L., and Moore, N. (2011). A spatial regression analysis of the influence of topography on monthly rainfall in east africa. *Int. J. Climatol.* 31, 1440–1456. doi: 10.1002/joc.2174

Huggett, J., Adetunji, J., Longstaffe, F., and Wray, D. (2017). Mineralogical and geochemical characterisation of warm-water, shallow-marine glaucony from the tertiary of the london basin. *Clays Clay Minerals* 52, 25–50. doi: 10.1180/claymin.2017.052.1.02

Junginger, A., and Trauth, M. H. (2013). Hydrological constraints of paleo-lake suguta in the northern kenya rift during the african humid period (15–5 ka BP). *Global Planetary Change* 111, 174–188. doi: 10.1016/j.gloplacha.2013.09.005

Libbey, R. B., Longstaffe, F. J., and Flemming, R. L. (2013). Clay mineralogy, oxygen isotope geochemistry, and water/rock ratio estimates, Te Mihi area, Wairakei geothermal field, new zealand. *Clays Clay Minerals* 61, 204–217. doi: 10.1346/CCMN.2013.0610304

Lyons, R. P., Scholz, C. A., Cohen, A. S., King, J. W., Brown, E. T., Ivory, S. J., et al. (2015). Continuous 1.3-million-year record of east african hydroclimate, and implications for patterns of evolution and biodiversity. *Proc. Natl. Acad. Sci.* 112, 15568–15573. doi: 10.1073/pnas.1512864112

McDonough, W. F., and Sun, S. S. (1995). The composition of the earth. *Chem. Geol.* 120, 223–253. doi: 10.1016/0009-2541(94)00140-4

McLennan, S. M. (2001). Relationships between the trace element composition of sedimentary rocks and upper continental crust. *Geochem. Geophys. Geosyst.* 2:1021. doi: 10.1029/2000GC000109

Middelburg, J. J., van der Weijden, C. H., and Woittiez, J. R. (1988). Chemical processes affecting the mobility of major, minor and trace elements during weathering of granitic rocks. *Chem. Geol.* 68, 253–273. doi: 10.1016/0009-2541(88)90025-3

Moore, D., and Reynolds, R. (1997). *X-ray Diffraction and the Identification and Analysis of Clay Minerals*, Second Edn. Oxford, England: Oxford University Press.

Nesbitt, H., and Young, G. (1982). Early Proterozoic climates and plate motions inferred from major element chemistry of lutites. *Nature* 299, 715–717. doi: 10.1038/299715a0

Nesbitt, H. W. (1979). Mobility and fractionation of rare earth elements during weathering of a granodiorite. *Nature* 279, 206–210. doi: 10.1038/279206a0

Nesbitt, H. W., and Markovics, G. (1980). Chemical processes affecting alkalis and alkaline earths during continental weathering. *Geochim. et Cosmochim. Acta* 44, 1659–1666. doi: 10.1016/0016-7037(80)90218-5

Nicholson, S. (2016). The turkana low-level jet: mean climatology and association with regional aridity. *Int. J. Climatol.* 36, 2598–2614. doi: 10.1002/joc.4515

Nicholson, S. E. (2018). The ITCZ and the seasonal cycle over equatorial africa. *Bull. Am. Meteorol. Soc.* 99, 337–348. doi: 10.1175/BAMS-D-16-0287.1

Otto-Bliesner, B. L., Russell, J. M., Clark, P. U., Liu, Z., Overpeck, J. T., Konecky, B., et al. (2014). Coherent changes of southeastern equatorial and northern african rainfall during the last deglaciation. *Science* 346, 1223–1227. doi: 10.1126/science.1259531

Renaut, R. (1993). Zeolitic diagenesis of late quaternary fluviolacustrine sediments and associated calcrete formation in the lake bogoria basin, kenya rift valley. *Sedimentology* 40, 271–301. doi: 10.1111/j.1365-3091.1993.tb01764.x

Roberts, N., Taieb, M., Barker, P., Damnati, B., Icole, M., and Williamson, D. (1993). Timing of the younger dryas event in east africa from lake-level changes. *Nature* 366, 146–148. doi: 10.1038/366146a0

Savin, S., and Lee, M. (1988). Isotopic studies of phyllosilicates. *Rev. Mineral. Geochem.* 19, 189–223.

Shanahan, T. M., McKay, N. P., Hughen, K. A., Overpeck, J. T., Otto-Bliesner, B., Heil, C. W., et al. (2015). The time-transgressive termination of the african humid period. *Nat. Geosci.* 8, 140–144. doi: 10.1038/ngeo2329

Singer, A., and Stoffers, P. (1980). Clay mineral diagenesis in two east african lake sediments. *Clays Clay Minerals* 15, 291–307. doi: 10.1180/claymin.1980.015.3.09

Sun, L., Semazzi, F. H., Giorgi, F., and Ogallo, L. (1999). Application of the NCAR regional climate model to eastern africa: 1. Simulation of the short rains of 1988. *J. Geophys. Res. Atmospheres* 104, 6529–6548. doi: 10.1029/1998JD200051

Surdam, R. C., and Eugster, H. P. (1976). Mineral reactions in the sedimentary deposits of the lake magadi region, kenya. *Geol. Soc. Am. Bull.* 87, 1739–1752. doi: 10.1130/0016-7606197687<1739:MRITSD<2.0.CO;2

Tian, J., Xie, X., Ma, W., Jin, H., and Wang, P. (2011). X-ray fluorescence core scanning records of chemical weathering and monsoon evolution over the past 5 Myr in the southern south china sea. *Paleoceanography* 26,

Tierney, J. E., and deMenocal, P. B. (2013). Abrupt shifts in horn of africa hydroclimate since the last glacial maximum. *Science* 342, 843–846. doi: 10.1126/science.1240411

Trauth, M. H., Deino, A., Bergner, A. G. N., and Strecker, M. R. (2003). East african climate change and orbital forcing during the last 175 kyr BP. *Earth Planetary Sci. Lett.* 206, 297–313. doi: 10.1016/S0012-821X(02)01105-6

Trauth, M. H., Deino, A., and Strecker, M. R. (2001). Response of the east african climate to orbital forcing during the last interglacial (130-117 kyr BP) and the early last glacial (117-60 kyr BP). *Geology* 29, 499–502. doi: 10.1130/0091-76132001029<0499:ROTEAC<2.0.CO;2

Viehberg, F. A., Just, J., Dean, J. R., Wagner, B., Franz, S. O., Klasen, N., et al. (2018). Environmental change during MIS4 and MIS 3 opened corridors in the horn of africa for homo sapiens expansion. *Quat. Sci. Rev.* 202, 139–153. doi: 10.1016/j.quascirev.2018.09.008

Conflict of Interest: The authors declare that the research was conducted in the absence of any commercial or financial relationships that could be construed as a potential conflict of interest.